# An emergent sea ice floe size distribution in a global coupled ocean–sea ice model

**Lettie A. Roach**[1,2], **Christopher Horvat**[*1,3], **Samuel M. Dean** [1] **and Cecilia M. Bitz**[4]

[1]National Institute of Water and Atmospheric Research, Wellington, NZ
[2]Victoria University of Wellington, Wellington, NZ
[3]Harvard University, Cambridge, MA, USA
[4]University of Washington, WA, USA

**Key Points:**

- We develop the first global ocean–sea ice model to prognostically simulate a sea ice floe size distribution
- The floe size distribution emerges by resolving processes acting on individual floes
- Floe-size dependent feedbacks have a significant impact on simulated sea ice

*Current affiliation: Brown University, Providence, RI, USA

Corresponding author: Lettie Roach, Lettie.Roach@niwa.co.nz

## Abstract

Sea ice is composed of discrete floes, which range in size across orders of magnitude. Here, we present a model that represents the joint distribution of sea ice thickness and floe size. Unlike previous studies, we do not impose a particular form on the subgrid-scale floe size distribution. Floe sizes are determined prognostically by the interaction of five key physical processes: new ice formation, welding of floes in freezing conditions, lateral growth and melt, and fracture of floes by ocean surface waves. Coupled model results suggest that these processes capture first-order characteristics of the floe size distribution, including decay in the distribution with increasing floe size and basin-wide spatial variability in representative radius. Lateral melt and floe welding are particularly important, with wave fracture creating floes at preferred sizes. The addition of floe size dependence to the existing model physics results in significant reductions in sea ice concentration, particularly in summer and principally due to floe-size-dependent lateral melt. The increased lateral melt alters partitioning of the melting potential, which reduces basal melt and increases sea ice thickness in some locations. These results suggest that including a floe size distribution may be important for accurate simulation of the polar climate system.


## 1 Introduction

The Earth's sea ice cover is a heterogeneous and variable medium, comprised of myriad individual solid pieces, called *floes*, each identifiable with a horizontal size. Sizes of individual floes vary over an extremely broad range, from centimeters to hundreds of kilometers. The floe size distribution (FSD), $F(r)$, is a probability function that characterizes this variability [*Rothrock and Thorndike*, 1984]. Over a region of the ice-covered ocean, $F(r)\mathrm{d}r$ is the fraction of a region covered by floes with a size between $r$ and $r + \mathrm{d}r$. Floe size has an important relationship with simulated sea ice evolution [*Steele*, 1992; *Horvat et al.*, 2016; *Rynders et al.*, 2016], which may be particularly relevant for the largely seasonal Antarctic sea ice cover, and as the Arctic ocean transitions from a perennial sea ice cover to a seasonal one [*Aksenov et al.*, 2017].

Current sea ice models are complex, incorporating multiple vertical layers in the snow and ice through which radiation scatters, variable surface treatments such as snow cover and melt ponds, and visco-plastic or elastic-brittle material properties that affect the ice deformation into ridges. Most describe the time evolution of ice using a probability distribution of ice in thickness categories following [*Thorndike et al.*, 1975]. To date no modern global climate models simulate floe size or the FSD. Recently, pan-Arctic [*Zhang et al.*, 2016] and stand-alone [*Bennetts et al.*, 2017] models which include floe size information have been demonstrated, but these impose the FSD shape or behavior rather than allowing it to emerge from physical processes acting on individual floes. Further, the power-law FSD profiles used to develop these empirical parametrizations may be inconsistent with observations [*Herman*, 2010] and the physics of sea ice floes [*Horvat and Tziperman*, 2017; *Herman et al.*, 2018].

In this study, we allow the FSD to emerge from the interaction of a set of coupled processes, rather than imposing a particular distributional shape. Building from the model of the joint floe size and thickness distribution (FSTD) developed by *Horvat and Tziperman* [2015, 2017], we present the first global ocean–sea ice model to prognostically simulate the sea ice FSD. The scheme is compatible with existing sea ice thickness distribution models and is implemented within the Los Alamos sea ice model, CICE5.1 [*Hunke et al.*, 2015]. The model simulates the statistical evolution of floes subject to lateral growth and melt, welding of floes in freezing conditions, new ice formation and fracture of floes by ocean surface waves, with the shape of the FSD emerging from these processes. Using the model in coupled ocean–sea ice simulations, we examine the contribution of those pro-

cesses to FSD evolution at a hemispheric scale. We further show that including floe size information has a significant impact on sea ice concentration and thickness globally.

This paper proceeds as follows: we discuss the incorporation of a prognostic FSD into CICE in Sec. 2. We show results from coupled simulations in Sec. 3; discuss limitations, compare to other studies, and make recommendations for observations that would advance FSD models in Sec. 4; and conclude in Sec. 5

## 2 Model

### 2.1 Standard model

The FSD model is implemented as a component of the Los Alamos sea ice model, CICE5.1 [*Hunke et al.*, 2015]. CICE ordinarily simulates an ice-thickness distribution (ITD), $g(h)$ (units $\mathrm{m}^{-1}$), where $g(h)\mathrm{d}h$ is defined as the fraction of ocean surface covered by ice with thickness between $h$ and $h + \mathrm{d}h$, such that

$$\int_0^{h_{\max}} g(h)\mathrm{d}h = 1. \tag{1}$$

The sea ice concentration, $c$, is obtained by integrating over all non-zero thicknesses resolved,

$$\int_{h_{\min}}^{h_{\max}} g(h)\mathrm{d}h = c, \tag{2}$$

where $h_{\min}$ is the lower bound of the smallest ice thickness class resolved. The sea ice concentration, $c$, and the open water fraction, $\phi$, sum to unity. The evolution of the ITD is,

$$\frac{\partial g}{\partial t} = -\frac{\partial}{\partial t}(\mu g) - \nabla \cdot (g\mathbf{v}) + \psi, \tag{3}$$

where terms on the right hand side, respectively, represent the change in thickness due to thermodynamic growth/melt at a melting/freezing rate $\mu(h)$; advection of the ice thickness distribution by sea ice dynamics at ice velocity $\mathbf{v}$; and redistribution of ice between thickness categories caused by sea ice deformation, $\psi$. We briefly describe the treatment of sea ice thermodynamics in CICE here.

The heat available in the surface ocean to melt or freeze sea ice is denoted $F_{\mathrm{frzmlt}}$ (units $\mathrm{W/m^2}$), and when $F_{\mathrm{frzmlt}} < 0$, the sea ice melts. Ice thickness changes at the ice base are determined by balancing the the conductive heat flux at the bottom surface, $F_{cb}$, and the net downward heat flux from the ice to the ocean, $F_{\mathrm{bot}}$ [*Maykut and McPhee*, 1995],

$$F_{\mathrm{bot}} = -c_p^{\mathrm{ocn}} \rho_w C_h u_* (T_w - T_f), \tag{4}$$

where $c_p^{\mathrm{ocn}}$ and $\rho_w$ are the ocean heat capacity and density, $C_h$ is a heat transfer coefficient, $u_*$ is the ocean-ice friction velocity, $T_f$ is the freezing temperature and $T_w$ is the ocean surface temperature.

Lateral sea ice melting is obtained as a function of a fixed floe size parameter, $L$. CICE uses a single floe size of $L \equiv 300$ m, which is an order of magnitude larger than the scale at which lateral melting is believed to affect sea ice volume evolution [*Steele*, 1992]. The change in sea ice concentration due to lateral melt follows *Steele* [1992],

$$\frac{\mathrm{d}g(h)}{\mathrm{d}t} = \frac{g(h)}{L} w_{\mathrm{lat}}, \tag{5}$$

with a vertically-averaged lateral melt rate, $w_{\mathrm{lat}}$, that is assumed to be uniform around the perimeter of each floe, given by *Josberger and Martin* [1981],

$$w_{\mathrm{lat}} = m_1 (T_w - T_f)^{m_2}. \tag{6}$$

The coefficients $m_1$ and $m_2$ are the best fit to data quoted by *Maykut and Perovich* [1987], measured in a single static lead in the Canadian Arctic archipelago over a three week period. The sum of $F_{\text{bot}}$ and the heat required to effect the change in concentration due to lateral melt, $F_{\text{side}}$, cannot exceed the melting potential, $F_{\text{frzmlt}}$, and are reduced proportionally if this occurs.

During freezing conditions, when $F_{\text{frzmlt}} \geq 0$, a volume of sea ice, $V_{\text{new}}$, is produced in proportion to $F_{\text{frzmlt}}$. This volume is added to the thinnest category, provided $V_{\text{new}}/\phi \leq 0.9h_1'$, where $h_1'$ is the upper boundary of the thinnest category. The fractional coverage of the thinnest category is increased by $\min(\phi, V_{\text{new}}/0.05\text{ m})$. However, if $V_{\text{new}}/\phi > 0.9h_1'$, then a volume $0.9h_1'\phi$ is added to the thinnest category and its fractional coverage is raised by $\phi$, and the surplus volume $V_{\text{new}} - 0.9h_1'\phi$ is distributed to all other thickness categories in proportion to their fractional coverage.

### 2.2 The joint floe size and ice thickness distribution

We extend the definition of the ice-thickness distribution following *Horvat and Tziperman* [2015] to a joint floe size and thickness distribution (FSTD). Individual floes are identified with a size $r$ and area $x(r)$, where $x(r) = 4\alpha r^2$ for $\alpha = 0.66 < \pi/4$ [*Rothrock and Thorndike*, 1984]. The probability distribution $f(r,h)\mathrm{d}r\mathrm{d}h$ is the fraction of grid surface area covered by ice with thickness between $h$ and $h + \mathrm{d}h$ and lateral floe size between $r$ and $r + \mathrm{d}r$. The FSTD satisfies

$$\int_{r_{\min}}^{r_{\max}} \int_0^{h_{\max}} f(r,h)\mathrm{d}r\mathrm{d}h \equiv \int_{\mathcal{R}} \int_{\mathcal{H}} f(r,h)\mathrm{d}r\mathrm{d}h = 1. \tag{7}$$

Integrating the FSTD over all floe sizes yields the ITD,

$$\int_{\mathcal{R}} f(r,h)\mathrm{d}r = g(h), \tag{8}$$

whereas integrating the FSTD over all ice thicknesses gives the FSD, $F(r)$,

$$\int_{\mathcal{H}} f(r,h)\mathrm{d}h = F(r). \tag{9}$$

We can also define the number FSTD, $f^N(r,h)$, where $f^N(r,h)\mathrm{d}r\mathrm{d}h$ is the number of floes per unit ocean surface area with thickness between $h$ and $h + \mathrm{d}h$ and lateral floe size between $r$ and $r + \mathrm{d}r$,

$$f^N(r,h) = \frac{f(r,h)}{4\alpha r^2}. \tag{10}$$

The number FSD, obtained by integrating $f^N(r,h)\mathrm{d}h$ over all ice thicknesses, is often used in observational studies (eg. *Perovich et al.* [2014]).

Following *Horvat and Tziperman* [2015], time evolution of the FSTD is given by

$$\frac{\partial f(r,h)}{\partial t} = -\nabla \cdot (f(r,h)\mathbf{v}) + \mathcal{L}_T + \mathcal{L}_M + \mathcal{L}_W. \tag{11}$$

The terms on the right hand side represent forcing of the distribution $f(r,h)$ by advection, thermodynamics, mechanical interactions between floes (ridging and rafting), and fracture by ocean surface waves, respectively.

To implement this model in CICE, we define a modified areal FSTD (mFSTD), $L(r,h)$, where, within a given thickness range between $h$ and $h + \mathrm{d}h$, $L(r,h)\mathrm{d}r$ is the fraction of ice with lateral floe size between $r$ and $r + \mathrm{d}r$. By definition, this satisfies

$$\int_{\mathcal{R}} L(r,h)\mathrm{d}r = 1, \tag{12}$$

and

$$f(r,h) = g(h)L(r,h). \tag{13}$$

Implementation of the mFSTD allows preservation of the standard model formulation for the ITD.

We neglect the two-way relationship between floe size and mechanical redistribution, retaining the standard CICE scheme for mechanical redistribution used to evolve the ITD. Mechanical redistribution reduces the area fractions of all floes equally, without affecting the mFSTD. Transport of the FSTD is achieved using the standard CICE scheme for tracer advection. The sizes of floes do not appear directly in any terms in the momentum equation or constitutive law. In reality, we would expect floe sizes to affect both mechanical redistribution and transport of the FSTD, but the precise relationships are uncertain and we assume that they are of second-order importance to simulation of the FSD.

Apart from advection, the processes which determine the FSTD are thermodynamics - lateral melt and growth, freezing-together of floes, and new ice formation - and mechanical wave fracture. These are described in more detail below.

### 2.3 Thermodynamics

Thermodynamic changes to the FSTD are given by

$$\mathcal{L}_T(r,h) = -\nabla_{(r,h)} \cdot (f(r,h)\mathbf{G}) + \frac{2}{r} f(r,h) G_r + \delta(r - r_{\min})\delta(h - h_{\min})\dot{A}_p + \beta_{\text{weld}}. \tag{14}$$

The first two terms on the right-hand side in Eqn. 14 represent growth and melt of existing floes in thickness and lateral size, at a rate $\mathbf{G} = (G_r, G_h)$. The third term represents growth of new ice: new floes are created at a rate $\dot{A}_p$ in the smallest thickness category $h_{\min}$, and the smallest lateral size category $r_{\min}$, i.e. that all ice forms initially as pancakes. To allow for the joining of individual floes to one another, we represent the welding together of floes in freezing conditions via the fourth term, $\beta_{\text{weld}}$.

In melting conditions, the lateral melt rate is

$$G_r = w_{\text{lat}} \tag{15}$$

to preserve consistency with the standard model, with $w_{\text{lat}}$ determined via Eqn. 6.

In freezing conditions, the lateral growth rate is

$$G_r = A_{\text{lat}} V_{\text{new}} / \Delta t, \tag{16}$$

where $\Delta t$ is the time step and $V_{\text{new}}$ is the volume of new ice growth in $\Delta t$, as per the standard model. $A_{\text{lat}}$ is the fraction of new ice growth that is taken to adhere to floe edges, representing lateral growth of existing floes. This is related to the “lead region", the area comprised of all annuli of width $r_{lw}$ (Table 1) around floes. The fraction of the domain belonging to the lead region, $\phi_{\text{lead}}$, is

$$\phi_{\text{lead}} = \min\left[\int_{\mathcal{R}}\int_{\mathcal{H}} f(r,h)\left(\frac{2r_{lw}}{r} + \frac{r_{lw}^2}{r^2}\right)\mathrm{d}r\mathrm{d}h, \phi\right]. \tag{17}$$

where $\phi$ is the open water fraction. Noting that the circumference of a floe is $4\alpha \cdot 2r$, the total lateral surface area of floes, per unit area of the ocean surface, is,

$$\overline{2hr} = \int_{\mathcal{R}}\int_{\mathcal{H}} f^N(r,h) 8\alpha r h \mathrm{d}r\mathrm{d}h.$$

Then the fraction of new ice growth adhering to floe edges, $A_{\text{lat}}$, is the product of the lead region with the fractional contribution of lateral surface area to the total surface area,

$$A_{\text{lat}} = \phi_{\text{lead}} \frac{\overline{2hr}}{\overline{2hr} + c}.$$

The volume that remains after lateral growth, $(1 - A_{\text{lat}})V_{\text{new}}$, is distributed according to the standard CICE new ice growth formulation as described in Subsec. 2.1. We choose to place newly formed ice in the smallest floe size category, parametrizing them as pancake floes, as mentioned above. See Sec. 4 for discussion of this choice.

Floes that are determined to be in contact with one another while the upper ocean is being cooled may freeze together [*Shen and Ackley*, 1991], a process that is dominant in the Southern Ocean [*Wadhams et al.*, 1987]. We consider sea ice floes randomly placed on the model domain and allow them to weld together thermodynamically during freezing conditions according to the probability that they overlap. For simplicity, we briefly change variables to floe area $x = 4\alpha r^2$ defined on $\mathcal{X} = [x_{\min}, x_{\max}]$, and presume sea ice is all of the same thickness. We define the area number density function $N(x)$ (units $\text{m}^{-4}$), with $N(x)\text{d}x$ equal to the number of floes per unit area between floe area $x$ and $x + \text{d}x$, noting that the area fraction occupied by floes with area between $x$ and $x + \text{d}x$ is $x \cdot N(x)\text{d}x$. The geometric probability of overlap is described using a "coagulation equation" [*Smoluchowski*, 1916; *Filbet and Laurençot*, 2004],

$$\frac{\partial N(x,t)}{\partial t} = \frac{1}{2}\int_{\mathcal{X}} K(x', x - x')\text{d}x' - \int_{\mathcal{X}} K(x, x')\text{d}x'. \tag{18}$$

$K(a, b)$ (units $\text{m}^{-6}s^{-1}$) is the "coagulation kernel", where $K(a, b)\text{d}a\text{d}b\text{d}t$ is the number of mergers per unit area of floes with area between $a$ and $a + \text{d}a$, and $b$ and $b + \text{d}b$ over a period $\text{d}t$, and $K(a, b) \equiv 0$ for any $a, b \leq 0$. The first integral in Eqn. 18 accounts for the formation of floes of area $x$ resulting from the merger of two floes with respective areas $x'$ and $x - x'$, where $x' < x$. The second integral describes the loss of floes with area $x$ by coagulation with other floes. We compute the coagulation kernel $K(x, x')$ as the product of the area fraction of floes of size $x$ and $x'$,

$$K(x, x') = \kappa \cdot x \cdot x' \cdot N(x)N(x'), \tag{19}$$

where $\kappa$ is a rate per unit area. Integrating Eqn. 18 over all $x$ leads to the time change of floe number per unit area, $\mathcal{N}$,

$$\begin{aligned}
\frac{\partial \mathcal{N}}{\partial t} &= \kappa \left[ \int_{\mathcal{X}} \text{d}x \int_{\mathcal{X}} \left( \frac{1}{2} x'(x - x')N(x')N(x - x') - xx'N(x)N(x') \right) \text{d}x' \right] \\
&= \frac{\kappa}{2} \left[ \int_{x_{\min}}^{x} \text{d}x' \left( \int_{\mathcal{X}} x'(x - x')N(x')N(x - x')\text{d}x \right) - 2c^2 \right] \\
&= -\frac{\kappa}{2} c^2,
\end{aligned}$$

where we make use of the fact that $\int xN(x)\text{d}x = c$. The rate per unit area $\kappa$ is the total number of floes that weld with another, per square meter, per unit time, in the case of a fully covered ice surface ($c = 1$), equal to twice the reduction in total floe number. *Roach et al.* [2018a] found a lower bound on $\kappa$ of 0.001 $\text{m}^{-2}\text{s}^{-1}$ in observations of small floes freezing together in the autumn Arctic Ocean. We use a value of $\kappa = 0.01$ $\text{m}^{-2}\text{s}^{-1}$ for the floe welding parameter.

### 2.4 Wave fracture

Following *Horvat and Tziperman* [2015], the change in the FSTD $f(r, h)$, per unit time due to fracture by ocean surface waves is,

$$\mathcal{L}_W(r, h) = -\Omega(r, h) + \int_{\mathcal{R}} \int_{\mathcal{H}} \Omega(s, h_s)\zeta(r, h, s, h_s)\text{d}s\text{d}h_s. \tag{20}$$

$\Omega(r, h)\text{d}r\text{d}h$ is the fraction of ocean surface area covered by floes with size and thickness between $(r, h)$ and $(r + \text{d}r, h + \text{d}h)$ that is fractured by waves per unit time. $\zeta(r, h, s, h_s)\text{d}r\text{d}h$ is the fraction of ocean surface area covered by floes with size and thickness between

$(r, h)$ and $(r + \mathrm{d}r, h + \mathrm{d}h)$ formed due to the fracture of floes with size and thickness between $(s, h_s)$ and $(s + \mathrm{d}s, h_s + \mathrm{d}h_s)$. The first term on the right-hand side in Eqn. 20 thus represents the fracture of floes at a given size and thickness into smaller sizes, and the second term represents the fracture of floes at larger sizes that result in floes at a given size and thickness.

We proceed by calculating the fractures that would occur if waves enter a fully ice-covered region defined in one dimension in the direction of propagation, and then apply the outcome proportionally to the ice-covered fraction in each grid cell. Noting that floe size is half its diameter, the sum of floe sizes in a one-dimensional, fully ice-covered domain is equal to the half the domain length, $D/2$. We consider the histogram of floe sizes, $W(r)$, formed due to the fracture of sea ice by waves, where $W(r)\mathrm{d}r$ is equal to the number of fractures with a resulting floe size between $r$ and $r + \mathrm{d}r$,

$$\int_{\mathcal{R}} rW(r)\mathrm{d}r = D/2. \tag{21}$$

The function $\zeta(r, h, s, h_s)$ is the fraction of $D$ composed of fractures of size $r$, equal to $rW(r)$ if $r < s$, and zero otherwise,

$$\zeta(r, h, s, h_s) = \frac{rW(r)}{\int_{r_{\min}}^{s} rW(r)\mathrm{d}r}\delta(h - h_s)\Theta(s - r) \tag{22}$$

where $\Theta$ is the Heaviside step function. By definition,

$$\int_{\mathcal{R}}\int_{\mathcal{H}} \zeta(r, h, s, h_s)\mathrm{d}r\mathrm{d}h = 1, \tag{23}$$

so Eqn. 20 conserves sea ice area and volume. We compute the area of floes of size $(r, h)$ that is fractured per unit time as

$$\Omega(r, h) = f(r, h)\frac{c_g}{D}\left(\frac{1}{D/2}\int_{r_{\min}}^{r} r'W(r')\mathrm{d}r'\right), \tag{24}$$

the product of three terms: (1) the fraction of ocean surface area originally covered by floes of size $(r, h)$; (2) the fraction of the domain that is reached by ocean surface waves moving at their group velocity $c_g$, $(c_g/D)$; and (3) the fraction of a fully-ice covered domain of width $D$ that would be fractured into radii smaller than $r$.

It remains to compute the histogram of new floe sizes $W(r)$, for which we require the sea surface height field $\eta(x)$. In the absence of a coupled wave model that simulates wave attenuation in ice, we construct an approximate attenuated sea surface height field using hindcast wave data outside the sea ice region. We neglect swell induced by winds within the ice pack and only draw in ocean swell along lines of constant longitude. In each ice-covered grid cell, we find the closest equatorward non-ice covered grid cell along lines of constant longitude. If this grid cell is land, no wave fracture occurs. If this grid cell is not land, we select the significant wave height and mean period from a wave model hindcast. The ocean wave spectrum is then constructed as a Bretschneider spectrum, following *Horvat and Tziperman* [2015] and *Bennetts et al.* [2017]. It is attenuated exponentially according to the number of floes in the grid cells between the ice-covered grid cell being considered and the non-ice-covered one. The attenuation coefficient is a quadratic function of sea ice thickness and wave period fit by *Horvat and Tziperman* [2015] to the results of *Kohout and Meylan* [2008]. Further information can be found in the Supplement of *Horvat and Tziperman* [2015].

From the local ocean surface wave spectrum we generate a realization of the sea surface height field using a random phase as in *Horvat and Tziperman* [2015]. Assuming

that sea ice flexes with the sea surface height field $\eta(y)$, strain $\epsilon$ is given by

$$\epsilon = \frac{h}{2}\frac{\partial^2 \eta}{\partial y^2}, \tag{25}$$

where $y$ is the spatial coordinate. The derivative is computed between successive extrema of the sea surface height, either (maximum, minimum, maximum) or (minimum, maximum, minimum). If the strain between successive extrema exceeds a critical value, $\epsilon_{\text{crit}}$ (Table 1), new floes are formed with diameters equal to the distance between the extrema. New floe radii resulting from fracture are collected into a histogram, $W(r)$, which depends only on the local sea surface height field. In the interests of computational expense, $W(r)$ and $c_g$ are computed offline for different values of sea ice thickness, mean wave period, significant wave height, and number of attenuating floes. This look-up table defines 5000 attenuated sea surface height fields which can be used to fracture ice during code integration. Given a sea surface height field, the scheme computes the new floe sizes generated by wave fracture explicitly, without requiring any assumptions about the FSD.

## 3 Results

The additional physics described in Subsec. 2.2-2.4 has been implemented in CICE5.1 [*Hunke et al.*, 2015] and coupled to the NEMO ocean model, using a configuration based on *Rae et al.* [2015]. The ocean–sea ice model is forced with the atmospheric reanalysis JRA-55 [*Japan Meteorological Agency*, 2013] and run on a $1^o$ tripolar grid. All simulations described here use repeated atmospheric forcing from a single year. We choose a pre-satellite era year (1975), as these spin-up simulations will be used to initialize transient simulations over the satellite era in later work. Wave forcing corresponding to the same year is taken from a hindcast of the ocean surface wave model, Wavewatch III [*Tolman*, 2009], which was also forced by JRA-55.

We present here two experiments: a simulation using the standard model (CICE5.1), and a simulation including a prognostic FSD as described above. All analysis uses monthly model output. Floe size categories follow a Gaussian spacing and span a similar range to those chosen by *Zhang et al.* [2015]. Finite differencing in floe size space follows the scheme used by *Hibler III* [1980] for finite differencing in thickness space.

Parameters which are not present in standard CICE and their values are shown in Table 1. As global observations of sea ice FSD are not available, parameter values have not been tuned or calibrated to reproduce certain FSD behavior and are based on estimates from previous studies. More information on the parameter values and their uncertainty can be found in the references provided in Table 1. In particular, *Horvat and Tziperman* [2015] performed local sensitivity tests for most parameters listed. As *Roach et al.* [2018a] suggest that their estimated lower bound for the floe welding parameter, $\kappa$, is conservative, we use a value that is one order of magnitude higher. $\kappa$ is the only new parameter presented here, so we include results from an experiment where its value is reduced in the Supplement. Grid-cell average floe sizes depend strongly on this parameter (see Supplement). Naturally, we expect floe sizes to also depend on the choice of floe size categories. More investigation of parameter sensitivity is required, but should occur in fully-coupled atmosphere-ocean simulations where all feedbacks are included—a step which is beyond the scope of this manuscript.

A key test of the new model physics is whether a sea ice FSD showing physically reasonable characteristics can be simulated in model experiments that begin without FSD initialization, sea ice cover and imposed FSD shape. All simulations are initialized without sea ice cover. Sea ice volume stabilizes after 15 years in the Arctic and after 45 years in the Antarctic. All further analysis is therefore conducted over the final twenty years of a 65 year model run. While detailed information is simulated at the sub-grid-scale, here we focus on resulting characteristics at the hemispheric scale to give an overall picture of

model behavior without focusing on any particular region. *Horvat and Tziperman* [2015, 2017] describe behavior of most processes included here at the sub-grid-scale. We proceed by first describing overall behavior of simulated floe size and then examining how different processes contribute to it.

To show floe size characteristics spatially at the hemispheric scale, we average over floe sizes. Fig. 1 shows the cell-average area-weighted 'representative' floe radius, $r_a$, which is defined using the areal FSTD,

$$r_a = \frac{\int_{\mathcal{R}} \int_{\mathcal{H}} r f(r,h) \mathrm{d}r \mathrm{d}h}{\int_{\mathcal{R}} \int_{\mathcal{H}} f(r,h) \mathrm{d}r \mathrm{d}h}. \tag{26}$$

The representative floe radius climatology in Fig. 1 is obtained after beginning the simulation without sea ice cover and allowing it to spin up. In the Northern Hemisphere (NH), the representative floe radius is largest in the centre of the ice pack and smaller towards the edges at the winter maximum in March (Fig. 1a). At the summer minimum in September, there are fewer very small and very large representative radii (Fig. 1b). Larger floes are concentrated around the coast near the Canadian archipelago and East Siberian sea. Generally, the representative floe radius is smaller in the Southern Hemisphere (SH) than the NH (Fig. 1c-d). In the winter, floes are largest in areas of compact ice, such as the Amundsen and Weddell Seas (Fig. 1d). In the summer, large floes are found on the edge of the ice cover (Fig. 1c).

Fig. 2a-d shows total hemispheric number distributions, which are obtained by integrating $f^N(r,h)$ over sea ice thickness and the ocean area in each hemisphere, for the NH in March (Fig. 2a), the NH in September (Fig. 2b), the SH in March (Fig. 2c) and the SH in September (Fig. 2d). The four total number distributions have a similar shape. A high number of small ($< 5$ m) floes is simulated all year, with more during the winter months than the summer months, due to the production of new pancake ice at the smallest resolved floe size. All four distributions in Fig. 2a-d show a significant fraction of floes in the largest floe size category ($> 750$ m), which arises from the truncation of floe size categories. The SH shows greater seasonal variation than the NH, with an order of magnitude more floes per unit area at nearly all sizes in March (Fig. 2c) than in September (Fig. 2d). The NH has more very large ($> 750$ m) floes per unit area than the SH. Some bending in the distribution is visible at floe sizes of around 100 m, particularly in the SH in September (Fig. 2d).

Fig. 2e-h show the tendencies arising from different floe processes in the total hemispheric number distributions, where the tendency in the number FSTD due to some process is defined as

$$\frac{\mathrm{d}f^N(r,h)}{\mathrm{d}t} = \frac{1}{\mathrm{d}t}(f(r,h)^N_{\text{after process}} - f(r,h)^N_{\text{before process}}), \tag{27}$$

and the model monthly output is the time average of $\frac{\mathrm{d}f(r,h)}{\mathrm{d}t}$. The tendencies at each floe size are the net result of floes being added to and removed from each floe size. Fig. 2f shows the NH in September and illustrates the general tendencies of the different processes. New ice growth creates very small floes; lateral growth and melt respectively act to increase and reduce the number at most sizes; wave fracture redistributes large floes to smaller sizes; and floe welding redistributes all floes to larger sizes.

Floe welding has the largest magnitude tendency of all five processes (Fig. 2e-h). Welding moves the smallest floes, created during new ice formation, to larger sizes and is the dominant process in the creation of very large floes. Fracture is a process that destroys large floes and produces smaller floes, so we expect the tendency of floe production to be negative for larger floes. In our simulation, the largest six floe sizes show a net loss due to wave fracture with a shape that is similar to their number distribution (but inverted). Sizes below around 150 m show a net gain, as large floes fracture into them, driving the

bending in the total floe number distribution at this size (Fig. 2a-d). Peaks around 100 m induced by wave fracture are balanced out by stronger freezing together of floes at that size in winter (Fig. 2e, h). Of the five processes, wave fracture has the most significant hemispheric difference, with net losses at some sizes below 100 m in the SH, unlike the NH.

Lateral melt is the dominant process to reduce floe sizes (Fig. 2e-h). It results in a net gain in the next-to-largest floe size category, due to the large number of floes in the largest floe size category (Fig. 2a-d). Lateral melt is around two orders of magnitude more important than lateral growth (Fig. 2e-h). Note that the model scheme directly couples lateral growth and new ice formation, such that if a larger portion of new ice went into lateral growth, fewer very small (< 5 m) floes would be created.

Fig. 3a-e show the tendency in representative radius,

$$\frac{\mathrm{d}r_a}{\mathrm{d}t} = \frac{\int_{\mathcal{R}}\int_{\mathcal{H}} r\frac{\mathrm{d}f(r,h)}{\mathrm{d}t}\mathrm{d}r\mathrm{d}h}{\int_{\mathcal{R}}\int_{\mathcal{H}} f(r,h)\mathrm{d}r\mathrm{d}h}, \tag{28}$$

hemispherically averaged for each process to give a sense of the seasonality of different processes. Wave fracture and lateral melt are much more impactful during the summer months than the rest of the year (Fig. 3a, e). During the summer months, there are more small floes (Fig. 1b-c), exposing more perimeter to lateral melt and allowing waves to penetrate deeper into the ice field. New ice growth climbs from zero just before the summer minimum and peaks two months after (Nov in the NH, Apr in the SH), gradually decreasing over the other months (Fig. 3b). Floe welding is strong all year outside of the summer months (JJA in the NH, DJF in the SH) (Fig. 3d).

Fig. 3f-o show the spatial variability of different processes, with each subplot showing the month where the net effect of each process is largest (according to Fig. 3a-e). For example, Fig. 3f shows lateral melt in the NH in July, which Fig. 3a shows is the month of largest impact. For all processes, the largest impacts occur around the ice edge (Fig. 3f-o). Floe welding is the only size-increasing process to have substantial impacts in the ice interior (Fig. 3i, n). It is the dominant driver in the creation of large floes (Fig. 2e-h) and thus controls the behavior of floe sizes in the central ice pack (Fig. 1a). Floe size reductions due to wave fracture occur along lines of constant longitude with few impacts in the central ice pack (Fig. 3j, o).

Of the five processes that determine the FSTD, only lateral melt, new ice formation and lateral growth directly change sea ice concentration, with lateral growth being the only of these not parametrized in the standard model. Yet even with these similarities to the standard model, the addition of a FSD results in significant changes to the standard model sea ice climatology. Fig. 4 shows the sea ice concentration simulated by the standard model and the difference between the standard and FSTD models. Only differences significant at the 95 % confidence level are shown. The inclusion of floe sizes generally acts to lower sea ice concentrations, particularly in already low-concentration areas. The average sea ice concentration reduction for regions that have reductions significant at the 95 % confidence level is −10 % in September in the NH and −40 % in March in the SH. At the ice edge, some of these represent total removal of ice in a grid cell. There are also small areas of increased concentrations at a similar magnitude to the decreases, such as the Weddell Sea (Fig. 4g). The small areas of increased concentrations tend to be near areas of increased ice advection. Overall, impacts are larger in the SH (Fig. 4g, h) than the NH (Fig. 4e, f), and in summer months (Fig. 4f, g) than winter months (Fig. 4e, h).

There are also significant differences when considering sea ice thickness. Fig. 5 shows the the grid cell mean thickness, which is the volume of ice per unit area, for the standard model and the difference between the standard and FSTD models. There are both increases and decreases in sea ice thickness relative to the standard model. The average reduction in the thickness of the ice-covered portion of grid cells (for regions that have

reductions significant at the 95 % confidence level) is −5 % (10 cm) in September in the NH and −12 % (13 cm) in March in the SH. Likewise, the average increase is 6 % (13 cm) in September in the NH and 25 % (23 cm) in March in the SH. Maximum increases and reductions in thickness are much greater at some locations.

Differences in lateral melt rates between the standard and FSTD models, which occur via the replacement of $L = 300$ m in Eqn. 5 with the distribution-integrated factor from Eqn. 14, are near-universally positive and coincide with areas of concentration decrease. Summing hemispherically, the total lateral melt rate increases approximately threefold in both hemispheres relative to the standard model (in September in the NH and March in the SH). This acts to reduce concentrations, and also allows some areas of increased frazil growth into the new open water.

Drawing a larger heat flux to melt ice laterally from the oceanic melting potential means that less is available for basal melt, which may contribute to thicker ice. The total hemispheric basal melt rate decreases by 20 % and 30 % in the NH in March and the SH in September respectively relative to the standard model. This reduction in basal melt occurs principally in areas of thick ice, where there is not much melting potential available to divide between basal and lateral melt. Therefore, areas of thick ice experience less basal melt in the FSTD model compared to the standard model, and so remain thicker throughout the year compared to the standard model. Areas of thin ice, where there is a higher melting potential, do not experience this basal melt reduction.

## 4 Discussion

The results presented here demonstrate that the inclusion of floe size information has a significant impact on sea ice concentration and thickness, in agreement with *Zhang et al.* [2016] and *Bennetts et al.* [2017]. The increase in lateral melt due to including a prognostic FSD reduces sea ice concentrations in both hemispheres, in an ocean–sea ice model with cyclic atmospheric forcing. This expanded model physics has the potential to alter sea ice feedbacks, climate sensitivity and the sea ice response to storms—impacts which will be investigated in future work.

The response of sea ice concentration and thickness to including prognostic floe size information in previous studies differ to those shown here, with both *Zhang et al.* [2016] and *Bennetts et al.* [2017] finding only reductions in sea ice thickness, and *Bennetts et al.* [2017] finding larger reductions in sea ice concentration than the present study. Differences between model configurations and forcing scenarios in the various studies mean that we cannot directly compare the impacts on sea ice concentration and thickness results at this stage.

The sea ice model described here includes a more comprehensive description of physical processes that affect sea ice floe size than those included in other studies. The lack of observations of the FSD covering a region and time period large enough for global model validation means that we cannot discern which model simulates the most realistic FSD. This lack of observational data is precisely what motivates our fully prognostic approach, rather than constraining the FSD based on minimal data as in *Zhang et al.* [2016] and *Bennetts et al.* [2017]. That we are able to capture some first-order characteristics of the FSD in our model experiments, which begin without initialization and allow the distribution to evolve freely, suggests that we have implemented some of the key physics that drive the FSD. These first-order characteristics include a varied spatial distribution of representative radius (Fig. 1), and a multi-scale number FSD (Fig. 2a-d) in line with observational studies (eg. *Steer et al.* 2008).

Our process-based approach to model development allows us to examine the contribution of different processes to the FSD, with insights that are useful for future model development. Such results cannot be obtained from reduced complexity models which tune

parametrizations to reproduce a certain FSD shape or behavior. While introducing additional uncertain parameters, we hope that consideration of individual physical processes will motivate further study and help prioritize parameters that require further observational constraints. Model results could inform development of parametrizations used in simpler models in the future. Below, we discuss the contribution of different processes to the FSD and their representation in current models, as well as highlighting areas that require further work.

We find that the freezing together of floes is a key process in determining the evolution of floe size (Fig. 2, 3). In previous modeling studies, the choice of how to include floe merging or welding has been ad-hoc: *Horvat and Tziperman* [2015] do not discuss welding; *Zhang et al.* [2016] move all floes into the largest category if the ice growth rate exceeds a threshold determined by tuning model output to observations in the western Arctic; and *Bennetts et al.* [2017] double the floe diameter in a grid cell if the ocean freezing potential is positive. Floe welding has only recently been quantified in the field for the first time by *Roach et al.* [2018a], who found observational support for use of the geometric floe welding model described here, but additional observations are required to better constrain the floe welding parameter.

The fracture of ice by ocean waves is also important, with preferred fracture sizes (eg. Fig. 2h) driving behavior in the number FSD (eg. Fig. 2d). We compute the new floe sizes generated by wave fracture explicitly, without requiring any assumptions about the FSD. In other parametrizations of wave fracture, *Zhang et al.* [2016] assume that wave-fractured ice is redistributed equally to all other categories of smaller size as a power law distribution. Their model depends strongly on a floe size redistribution "participation factor", which they parametrize as a function of wind speed and open water fraction, fitting tuning constants in their model to cumulative number distributions observed in satellite images in the western Arctic. In *Bennetts et al.* [2017], floes fracture according to a strain criterion similar to ours, but the change in the FSD is calculated assuming a "split power law" distribution of floes sizes based on observations from *Toyota et al.* [2011]. *Zhang et al.* [2016] and *Bennetts et al.* [2017] impose behavior on fractured floe sizes that is inconsistent with results from a small-scale model [*Montiel and Squire*, 2017] and laboratory observations [*Herman et al.*, 2018], which indicate preferred sizes in the FSD resulting from wave fracture. Developing or tuning models to explicitly match "split power law" shapes may be misleading, as many observations do not show a this distribution (eg. *Inoue et al.* [2004], *Wang et al.* [2016], *Paget et al.* [2001]). Further, observations of a "split power law" distribution could be interpreted as a gradual bending of curves rather than an abrupt transition [*Herman*, 2010].

In future work, the sea ice model should be coupled to a full spectrum ocean wave model with an appropriate treatment of wave energy damping by sea ice. There are certainly limitations with our attenuation scheme, which may not be suitable for small floes [*Meylan*, 2002] and neglects wave direction, unlike *Bennetts et al.* [2017]. Sensitivity of the depth of wave penetration into the pack ice using different attenuation parametrizations such as *Meylan et al.* [2014] could be tested with our model, either using forcing data from a wave model hindcast or coupled to a wave model. Wave model coupling would also allow turbulent mixing due to ocean waves to occur within the sea ice region, influencing the heat fluxes available for sea ice melt and growth. More realistic simulation of waves in ice could also enable advances in the representation of sea ice growth [*Roach et al.*, 2018a].

The choice of floe size assigned to new floes strongly impacts the simulated floe number distribution (Fig. 2). In our model, new ice is placed in the smallest floe size category, representing pancake ice formation. This results in large numbers of small floes during winter, a seasonality opposite to that obtained by *Zhang et al.* [2016]. In reality, new frazil ice is herded into pancake floes only in the presence of surface waves and/or winds, while in the absence of wind and wave action frazil crystals freeze together to form

large thin sheets of sea ice called nilas [*Weeks and Ackley*, 1986]. *Zhang et al.* [2016] do not specify how they initialize floe sizes at the start of their simulation, nor the floe sizes at which new ice forms. *Zhang et al.* [2015] perform simple experiments that are initialized at the largest floe size. *Bennetts et al.* [2017] initialize their model using a constant floe diameter of 300 m, and do not explain how the formation of new ice impacts the representative floe diameter. These models and the standard version of CICE could be considered to include nilas growth only. In contrast, our model includes pancake growth only, although the initial thickness of ice may correspond better to nilas growth than pancakes. Future models should ideally incorporate both nilas and pancake growth, perhaps using some critical value of the tensile stress mode arising from the wave field [*Shen et al.*, 2004] to determine which growth type occurs.

Of the five processes that determine the FSD, only new ice formation and lateral melt and growth cause changes to sea ice concentration in our model. We find that lateral growth, which was not included in either *Zhang et al.* [2016] or *Bennetts et al.* [2017], is around two orders of magnitude smaller overall than lateral melt (Fig. 2e-h). *Roach et al.* [2018a] find that the lateral growth model used here underestimates growth rates of small ice floes observed in the Arctic Ocean during fall. More observations are required to determine whether the model underestimates lateral growth rates in other conditions.

Here, lateral melting is a significant process for evolution of the sea ice FSD (Fig. 2e-h) and is a function of the FSD itself. In contrast, the lateral melt formulation in *Zhang et al.* [2016] assumes all floe size categories have the same ITD, and does not parametrize the effect of lateral melting on the FSD (the second term in Eqn. 14). *Bennetts et al.* [2017] use a single representative floe size in each grid cell, neglecting the sub-grid-scale distribution of floe sizes, which could vary over a broad range. All three models demonstrate that lateral melt has large impact on simulated sea ice concentration, also motivating further observational validation. As noted by *Roach et al.* [2018b], the parametrization of lateral melt rate used in our model and standard CICE5.1, as well as other models, is based on a single field study of a single floe [*Maykut and Perovich*, 1987]. Further constraints on individual processes like this, which strongly impact the sea ice FSD, could greatly assist model development, particularly in the absence of global observations of floe sizes.

## 5 Conclusions

In this study, we have presented a scheme for modeling a fully prognostic joint sea ice floe size and thickness distribution. We have examined model results in both hemispheres obtained without initialization or tuning parameters to obtain a particular floe size distribution, unlike previous studies. We find that the five processes implemented here—lateral melt and growth of floes, floe welding in freezing conditions, new ice formation and fracture of floes by ocean surface waves—capture some first-order characteristics of the floe size distribution.

However, definite statements on the realism of the simulated distribution are hindered by a lack of global observations of floe size distribution. Observations which cover a large spatial and temporal region at small enough resolution are not yet available. This lack of observations is the motivation for constructing a model which does not assume *a priori* distributions for simulated floe sizes. This general framework makes any additions or modifications to physical processes straightforward to implement. Future additions may include dynamics more appropriate for the marginal ice zone (eg. *Rynders et al.* 2016), floe-size-dependent mechanical redistribution (eg. *Horvat and Tziperman* 2015), dependence of form drag on the simulated floe size distribution, two clearly defined sea ice growth pathways (nilas and pancake growth), and coupling with an ocean wave model.

In spite of our choices to keep much of the physics consistent with the standard model, impacts on sea ice concentration and thickness caused by the addition of a floe size distribution are significant. This suggests that small scale processes associated with individual floes may be important for the polar climate system. The observed predominance of sea ice growth via pancake formation in the Antarctic [*Wadhams et al.*, 1987] suggests that these processes may be particularly relevant for the Southern Hemisphere. Moreover, the predicted increase in the Arctic marginal ice zone [*Aksenov et al.*, 2017] implies that processes at the sea ice floe scale may become more important for simulation of sea ice in the future. The model presented here could help to answer questions on the seasonal evolution of floe size in the polar oceans, the possibility of power law emergence from interactions at the floe scale in a climate model, and the degree to which sea ice melting is influenced by fractured sea ice cover.

572 **Table 1.** Parameters that are not present in standard CICE. $r_1$ denotes the smallest floe size resolved in the
573 model

| Parameter | Description | Value | Reference |
|---|---|---|---|
| $\alpha$ | Non-circularity of floes | 0.66 | *Rothrock and Thorndike* [1984] |
| $r_{lw}$ | Width of lead region | $r_1$ | *Horvat and Tziperman* [2015] |
| $\kappa$ | Rate constant for merging | 0.01 $m^{-2}$ $s^{-1}$ | *Roach et al.* [2018a] and see Supplement |
| $\epsilon_{\text{crit}}$ | Critical strain | $3 \times 10^{-5}$ | *Horvat and Tziperman* [2015] , *Kohout and Meylan* [200 |
| $t_{\text{wave}}$ | Smallest floe size affected by waves | 10 m | *Toyota et al.* [2011] |

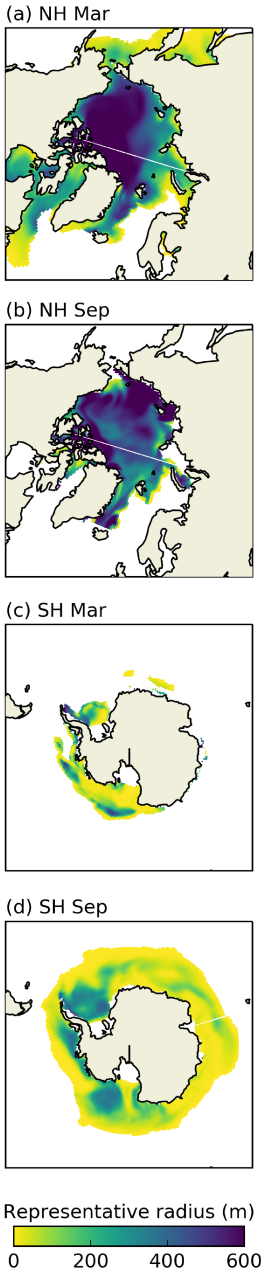


**Figure 1.** The simulated representative floe radius, averaged over twenty years following spin-up, in (a, c) March and (b, d) September, in (a, b) the Northern Hemisphere and (c, d) the Southern Hemisphere. The range displayed is chosen to display both hemispheres on the same scale; dark purple may be greater than 600 m.

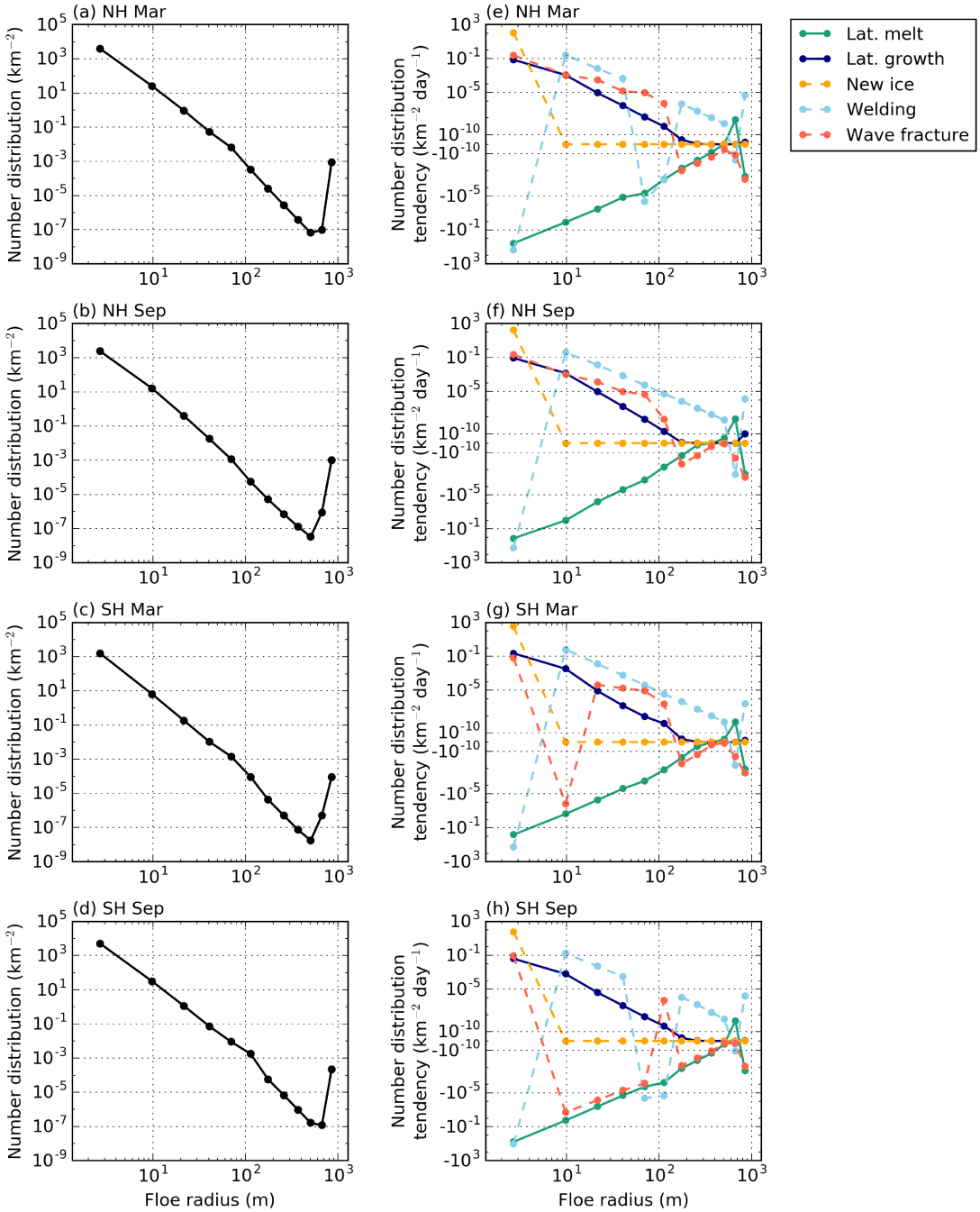


**Figure 2.** (a) The Northern Hemisphere floe number distribution in March averaged over the twenty years following model spin-up. (b-d) Same as (a), for the Northern Hemisphere in September, the Southern Hemisphere in March, and the Southern Hemisphere in September, respectively. (e) The net tendency in the floe number distribution from different physical processes in the Northern Hemisphere in March averaged over the twenty years following model spin-up. The axis in (e) is linearized around zero. (f-h) Same as (e), for the Northern Hemisphere in September, the Southern Hemisphere in March, and the Southern Hemisphere in September respectively.

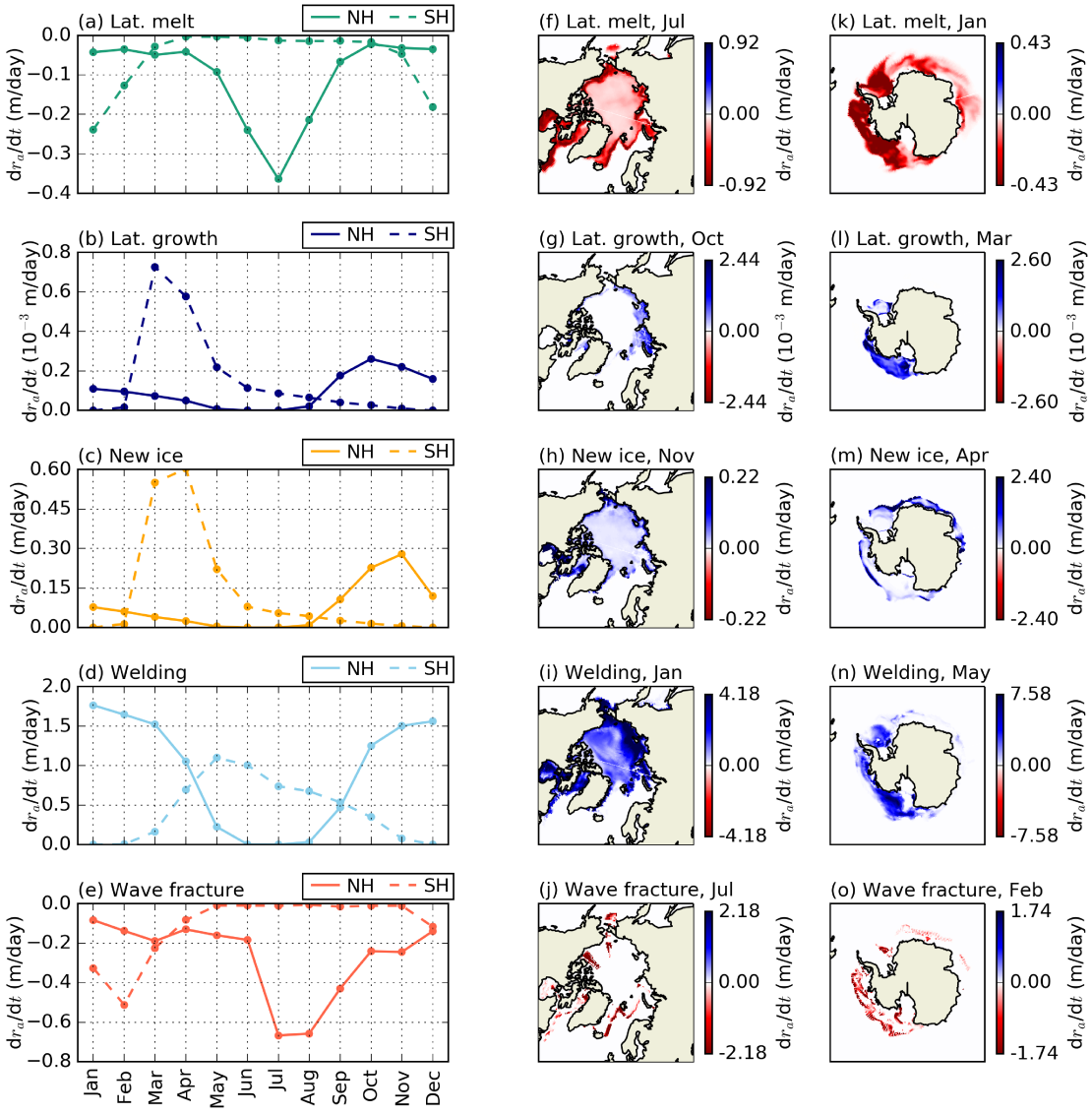


**Figure 3.** Seasonal and spatial variability of tendencies in representative radius, $r_a$. (a) The hemispheric average tendency in representative radius due to lateral melt for the NH (solid line) and SH (dashed line). (b-e) as (a) but for lateral growth, new ice production, floe welding, and wave fracture respectively. (f) Map of the tendency in $r_a$ due to lateral melt in the NH for the month with maximum average tendency, July, (see (a), solid line). (k) Map of the tendency in $r_a$ due to lateral melt in the SH for the month with maximum average tendency, January, (see (a), dashed line). (g-j) as (f) and (l-o) as (k) but for lateral growth, new ice production, floe welding, and wave fracture respectively. Note that lateral growth has units of $10^{-3}$ m day$^{-1}$, while other processes have units of m day$^{-1}$.

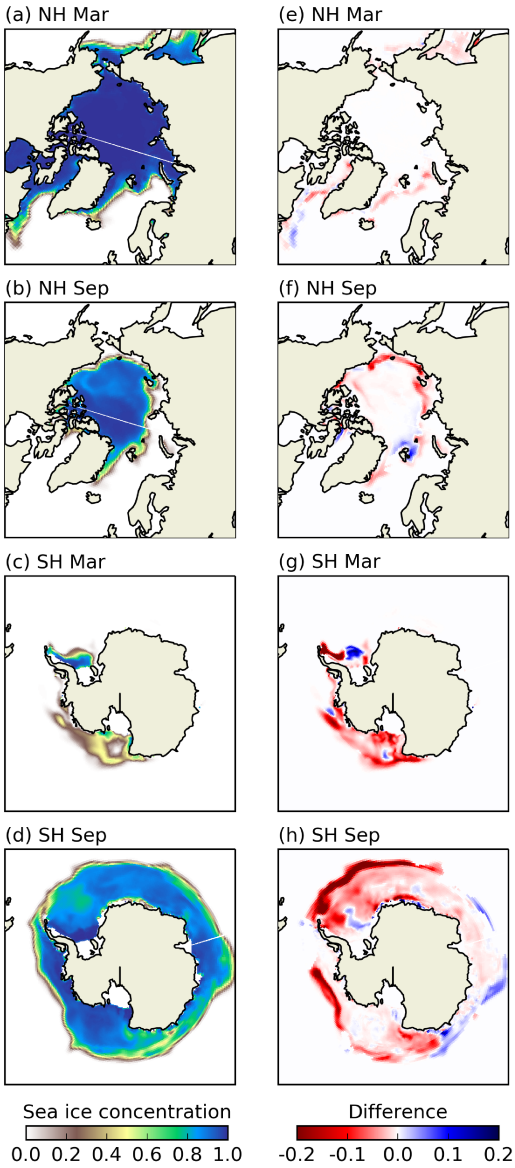


**Figure 4.** Monthly sea ice concentration fields (out of maximum of 1) averaged over twenty years in the Northern and Southern Hemispheres for March (a, c, e, g) and September (b, d, f, h). The first column (a-d) shows the simulation from the standard model and the second column (b-h) shows shows the difference between the standard and FSTD models, where only differences that are significant at the 95% confidence level are shown.

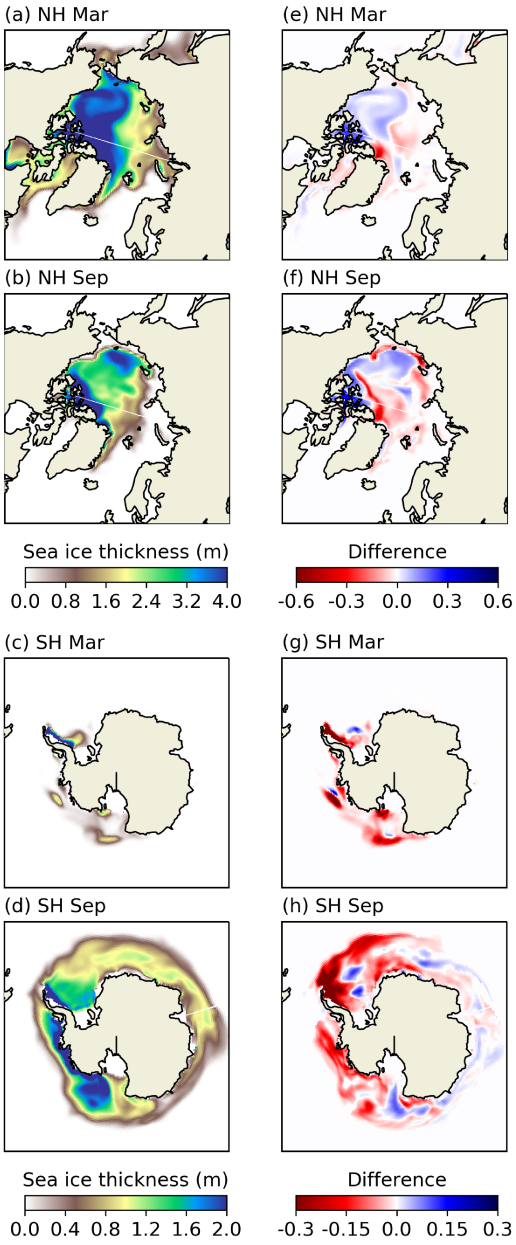


**Figure 5.** As Fig. 4, but for sea ice volume per unit area (in m).

**Acknowledgments**

LR and SD were funded via Marsden contract VUW-1408. CH was supported by the Frank Knox Memorial Fellowship during parts of this work. CMB was supported by the US National Science Foundation PLR-1643431. The authors would like to thank Richard Gorman for producing the wave model hindcast, Erik Behrens for setting up the standard model NEMO-CICE configuration, and Elizabeth Hunke and an anonymous reviewer for their consideration of the manuscript. The authors also wish to acknowledge the contribution of NeSI high-performance computing facilities to the results of this research. NZ's national facilities are provided by the NZ eScience Infrastructure and funded jointly by NeSI's collaborator institutions and through the Ministry of Business, Innovation & Employment's Research Infrastructure programme. Model results are publicly available via Zenodo, (https://doi.org/10.5281/zenodo.1193929).

## References

Aksenov, Y., E. E. Popova, A. Yool, A. J. G. Nurser, T. D. Williams, L. Bertino, and J. Bergh (2017), On the future navigability of Arctic sea routes: High-resolution projections of the Arctic Ocean and sea ice, *Mar. Policy.*, *75*, 300–317, doi: 10.1016/j.marpol.2015.12.027.

Bennetts, L. G., S. O'Farrell, and P. Uotila (2017), Brief communication: Impacts of ocean-wave-induced breakup of Antarctic sea ice via thermodynamics in a stand-alone version of the CICE sea-ice model, *Cryosphere*, *11*(3), 1035–1040, doi:10.5194/tc-11-1035-2017.

Filbet, F., and P. Laurençot (2004), Numerical simulation of the Smoluchowski coagulation equation, *SIAM Journal on Scientific Computing*, *25*(6), 2004–2028, doi: 10.1137/S1064827503429132.

Herman, A. (2010), Sea-ice floe-size distribution in the context of spontaneous scaling emergence in stochastic systems, *Physical Review E*, *81*(6), 66,123, doi: 10.1103/PhysRevE.81.066123.

Herman, A., K.-U. Evers, and N. Reimer (2018), Floe-size distributions in laboratory ice broken by waves, *The Cryosphere*, *12*, 685–699, doi:https://doi.org/10.5194/tc-12-685-2018.

Hibler III, W. D. (1980), Modeling a Variable Thickness Sea Ice Cover, *Monthly Weather Review*, *108*(12), 1943–1973, doi:10.1175/1520-0493(1980)108<1943:MAVTSI>2.0.CO;2.

Horvat, C., and E. Tziperman (2015), A prognostic model of the sea-ice floe size and thickness distribution, *The Cryosphere*, *9*(6), 2119–2134, doi:10.5194/tc-9-2119-2015.

Horvat, C., and E. Tziperman (2017), The evolution of scaling laws in the sea ice floe size distribution, *J. Geophys. Res. Ocean.*, *122*(9), 7630–7650, doi:10.1002/2016JC012573.

Horvat, C., E. Tziperman, and J.-M. Campin (2016), Interaction of sea ice floe size, ocean eddies and sea ice melting, *Geophys. Res. Lett.*, *43*(15), 8083–8090, doi: 10.1002/2016GL069742.

Hunke, E. C., W. H. Lipscomb, A. K. Turner, N. Jeffery, and S. Elliott (2015), CICE: the Los Alamos Sea Ice Model Documentation and Software User's Manual Version 5.1 LA-CC-06-012, *Tech. rep.*, Los Alamos National Laboratory, New Mexico, US.

Inoue, J., M. Wakatsuchi, and Y. Fujiyoshi (2004), Ice floe distribution in the Sea of Okhotsk in the period when sea-ice extent is advancing, *Geophys. Res. Lett.*, *31*(20).

Japan Meteorological Agency, J. (2013), JRA-55: Japanese 55-year Reanalysis, Daily 3-Hourly and 6-Hourly Data, *Tech. rep.*, Japan Meteorological Agency, Boulder, CO, doi: 10.5065/D6HH6H41.

Josberger, E. G., and S. Martin (1981), A laboratory and theoretical study of the boundary layer adjacent to a vertical melting ice wall in salt water, *Journal of Fluid Mechanics*, *111*, 439–473.

Kohout, A. L., and M. H. Meylan (2008), An elastic plate model for wave attenuation and ice floe breaking in the marginal ice zone, *J. Geophys. Res. Ocean.*, *113*(C09016), 1–17, doi:10.1029/2007JC004434.

Maykut, G. A., and M. G. McPhee (1995), Solar heating of the Arctic mixed layer, *J. Geophys. Res. Ocean.*, *100*(C12), 24,624–691,703, doi:10.1029/95JC02554.

Maykut, G. A., and D. K. Perovich (1987), The role of shortwave radiation in the summer decay of a sea ice cover, *J. Geophys. Res. Ocean.*, *92*(C7), 7032–7044, doi:10.1029/JC092iC07p07032.

Meylan, M. H. (2002), Wave response of an ice floe of arbitrary geometry, *J. Geophys. Res.*, *107*(C1,3005), 5–1–5–11, doi:10.1029/2000JC000713.

Meylan, M. H., L. G. Bennetts, and A. L. Kohout (2014), In situ measurements and analysis of ocean waves in the Antarctic marginal ice zone, *Geophys. Res. Lett.*, *41*(14), 5046–5051, doi:10.1002/2014GL060809.In.

Montiel, F., and V. A. Squire (2017), Modelling wave-induced sea ice breakup in the marginal ice zone, *Proc. R. Soc. A*, *473*, 1–32, doi:10.1098/rspa.2017.0258.

Paget, M. J., A. P. Worby, and K. J. Michael (2001), Determining the floe-size distribution of East Antarctic sea ice from digital aerial photographs, *Ann. Glaciol.*, *33*(1), 94–100.

Perovich, D., J. Richter-Menge, C. Polashenski, B. Elder, T. Arbetter, and O. Brennick (2014), Sea ice mass balance observations from the North Pole Environmental Observatory, *Geophys. Res. Lett.*, *41*(6), 2019–2025, doi:10.1002/2014GL059356.

Rae, J. G. L., H. T. Hewitt, A. B. Keen, J. K. Ridley, A. E. West, C. M. Harris, E. C. Hunke, and D. N. Walters (2015), Development of the Global Sea Ice 6.0 CICE configuration for the Met Office Global Coupled model, *Geosci. Model Dev.*, *8*(7), 2221–2230, doi:10.5194/gmd-8-2221-2015.

Roach, L. A., M. M. Smith, and S. M. Dean (2018a), Quantifying growth of pancake sea ice floes using images from drifting buoys, *J. Geophys. Res. Ocean.*, Accepted Author Manuscript. doi:10.1002/2017JC013693.

Roach, L. A., S. M. Dean, and J. A. Renwick (2018b), Consistent biases in Antarctic sea ice concentration simulated by climate models, *The Cryosphere*, *12*, 365–383, doi:https://doi.org/10.5194/tc-12-365-2018.

Rothrock, D. A., and A. S. Thorndike (1984), Measuring the sea ice floe size distribution, *J. Geophys. Res. Ocean.*, *89*(C4), 6477–6486, doi:10.1029/JC089iC04p06477.

Rynders, S., Y. Aksenov, D. Feltham, G. Nurser, and A. Naveira Garabato (2016), Modelling MIZ dynamics in a global model, in *EGU Gen. Assem. Conf. Abstr.*, p. 1004.

Shen, H. H., and S. F. A. Ackley (1991), A one-dimensional model for wave-induced ice-floe collisions, *Annals of Glaciology*, *15*(1), 87–95.

Shen, H. H., S. F. Ackley, and Y. Yuan (2004), Limiting diameter of pancake ice, *Journal of Geophysical Research: Oceans*, *109*(C12035), 1–13, doi:10.1029/2003JC002123.

Smoluchowski, M. V. (1916), Zur Theorie der Zustandsgleichungen, *Annalen der Physik*, *353*(24), 1098–1102, doi:10.1002/andp.19163532407.

Steele, M. (1992), Sea ice melting and floe geometry in a simple ice-ocean model, *J. Geophys. Res. Ocean.*, *97*(C11), 17,729–17,738.

Steer, A., A. Worby, and P. Heil (2008), Observed changes in sea-ice floe size distribution during early summer in the western Weddell Sea, *Deep Sea Res. Pt II*, *55*(8-9), 933-942, doi:10.1016/j.dsr2.2007.12.016.

Thorndike, A. S., D. A. Rothrock, G. A. Maykut, and R. Colony (1975), The thickness distribution of sea ice, *J. Geophys. Res. Ocean.*, *80*(33), 4501, doi:10.1029/JC080i033p04501.

Tolman, H. L. (2009), User manual and system documentation of WAVEWATCH III TM version 3.14, *Tech. rep.*, Environmental Modeling Center, NCEP, Camp Springs, MD 20746.

Toyota, T., C. Haas, and T. Tamura (2011), Size distribution and shape properties of relatively small sea-ice floes in the Antarctic marginal ice zone in late winter, *Deep Sea Res. Pt II*, *58*(9), 1182–1193, doi:10.1016/j.dsr2.2010.10.034.

Wadhams, P., M. Lange, and S. F. Ackley (1987), The ice thickness distribution across the Atlantic sector of the Antarctic Ocean in midwinter, *Journal of Geophysical Research: Oceans (1978–2012)*, *92*(C13), 14,535–14,552, doi:10.1029/JC092iC13p14535.

Wang, Y., B. Holt, W. E. Rogers, J. Thomson, H. H. Shen, W. Erick Rogers, J. Thomson, and H. H. Shen (2016), Wind and wave influences on sea ice floe size and leads in the Beaufort and Chukchi Seas during the summer-fall transition 2014, *J. Geophys. Res. Ocean.*, *121*(2), 1502–1525, doi:10.1002/2015jc011349.

Weeks, W. F. S., and S. F. Ackley (1986), *The growth, structure, and properties of sea ice*, vol. 146, 9–164 pp., Springer, Boston, MA, doi:10.1002/9781444317145.ch2.

Zhang, J., A. Schweiger, M. Steele, and H. Stern (2015), Sea ice floe size distribution in the marginal ice zone: Theory and numerical experiments, *J. Geophys. Res. Ocean.*, *120*(5), 3484–3498, doi:10.1002/2015JC010770.

Zhang, J., H. Stern, B. Hwang, A. Schweiger, M. Steele, M. Stark, and H. C. Graber (2016), Modeling the seasonal evolution of the Arctic sea ice floe size distribution, *Elem Sci Anth*, *4*(1), 126, doi:10.12952/journal.elementa.000126.